

# Probe knots and Hopf insulators with ultracold atoms

Dong-Ling Deng,<sup>1,2,3</sup> Sheng-Tao Wang,<sup>1,3</sup> Kai Sun,<sup>1</sup> and L.-M. Duan<sup>1,3</sup>

<sup>1</sup>*Department of Physics, University of Michigan, Ann Arbor, Michigan 48109, USA*

<sup>2</sup>*Condensed Matter Theory Center and Joint Quantum Institute,*

*Department of Physics, University of Maryland, College Park, MD 20742-4111, USA*

<sup>3</sup>*Center for Quantum Information, IIS, Tsinghua University, Beijing 100084, PR China*

**Knots and links are fascinating and intricate topological objects. Their influence spans from DNA and molecular chemistry to vortices in superfluid helium, defects in liquid crystals and cosmic strings in the early universe. Here, we find that knotted structures also exist in a peculiar class of three-dimensional topological insulators—the Hopf insulators. In particular, we demonstrate that the momentum-space spin textures of Hopf insulators are twisted in a nontrivial way, which implies the presence of various knot and link structures. We further illustrate that the knots and nontrivial spin textures can be probed via standard time-of-flight images in cold atoms as preimage contours of spin orientations in stereographic coordinates. The extracted Hopf invariants, knots, and links are validated to be robust to typical experimental imperfections. Our work establishes the existence of knotted structures in Hopf insulators, which may have potential applications in spintronics and quantum information processing.**

More than a century ago, Lord Kelvin propounded his celebrated “vortex atom” theory, which asserted that atoms are made of vortex knots in the aether [1]. Knot theory has since become a central subject in topology and began to undertake important roles in diverse fields of sciences. Biologists discovered that molecular knots and links in DNA are crucial in vital processes of replication, transcription and recombination [2, 3]. In supramolecular chemistry, complex knotted structures have been demonstrated in the laboratory [4–6] and were shown to be essential for the crystallization and rheological properties of polymers [7]. In physics, knot has appeared in many subfields, such as classical field theory [8, 9], helium superfluid [10], fluid mechanics and plasma [11], spinor Bose-Einstein condensates [12], chiral nematic colloids [13–15], quantum chromodynamics [16] and string theory [17]. Recently, exciting progresses are made in laboratories to observe the knots. Experimental creation of knotted configurations has been demonstrated in liquid crystal [18–21], laser light [22], fluid flows [23, 24], and spinor Bose-Einstein condensate [25], driving a new wave of interest in the study of knots.

In quantum condensed matter physics, topology is crucial in understanding exotic phases and phase transitions. Notable examples include the discoveries of the Berezinskii-Kosterlitz-Thouless transition [26, 27] and the quantum Hall effect [28]. More recently, another new class of materials, dubbed topological insulators, was theoretically predicted and experimentally observed [29–31]. In general, they are topological phases protected by system symmetries, which cannot be smoothly connected to the trivial phase if the respective symmetries are preserved [32]. For these materials, the nontriviality originates from the interplay between symmetry and topology. Many peculiar physical phenomena are predicted or observed in experiments, including, for instance, quan-

tized Hall conductance [33], robust chiral edge states [29], magnetic monopole [34], wormhole and Witten effects [35, 36]. However, despite these striking progresses, the relation between topological insulators and knot theory remains largely unexplored. It is unclear whether topological insulators carry nontrivial knot structures and how we can visualize these structures.

In this paper, we reveal intriguing knot and link structures hidden in a particular class of topological insulators. Specifically, we find various nontrivial knot and link structures encoded in the spin textures of Hopf insulators. Hopf insulators are special three-dimensional (3D) topological insulators without the need for symmetry protection [37, 38]. We show that in momentum space the spin textures of Hopf insulators represent special realizations of the long-sought-after Hopfions [8, 39], which are 3D topological solitons evading any experimental observation so far. Inspired by the rapid experimental progress of synthetic gauge fields in cold atoms [40–47], we propose a scheme to measure the Hopf topology and visualize different knots and links based on cold-atom technologies. We demonstrate how to extract the Hopf invariant and the knotted spin textures from the state-of-the-art time-of-flight imaging data. The corresponding knots and links are explicitly revealed as preimage contours of the observed spin orientations via a stereographic coordinate system. The extracted information—Hopf invariants, knots, and links—is robust against typical experimental imperfections. This work opens a new avenue for study of topological insulators and knot theory in ultracold atom experiments.

## Results

**Hopf insulators and knots.** Hopf insulators are 3D topological insulators characterized by an integer Hopf index and have topologically protected metallic surface

states [37, 38]. Unlike the recently predicted [48–50] and experimentally observed 3D  $\mathbb{Z}_2$  topological insulators with a time-reversal symmetry [51, 52], Hopf insulators do not require any symmetry protection (other than the prerequisite  $U(1)$  charge conservation). They are peculiar exceptions that sit outside of the periodic table for topological insulators and superconductors [53, 54]. One may regard them as a 3D generalization of the 2D quantum anomalous Hall effect [55]. A model Hamiltonian for the Hopf insulator with Hopf invariant  $\chi = \pm 1$  was first introduced by Moore, Ran and Wen [37]. In our previous works [38, 56], we generalized their results and constructed Hamiltonians for Hopf insulators with arbitrary Hopf index, using two different approaches, one based on the quaternion algebra [56] and the other based on the generalized Hopf map [38]  $f : \mathbb{S}^3 \rightarrow \mathbb{S}^2$  (up to irrelevant overall normalizations)

$$S_x + iS_y = 2\eta_\uparrow^p \bar{\eta}_\downarrow^q, \quad S_z = (|\eta_\uparrow|^{2p} - |\eta_\downarrow|^{2q}), \quad (1)$$

where  $\mathbb{S}^2$  and  $\mathbb{S}^3$  denote respectively the 2D and 3D spheres, the  $\mathbb{S}^3$  coordinates  $\boldsymbol{\eta} = (\text{Re}[\eta_\uparrow], \text{Im}[\eta_\uparrow], \text{Re}[\eta_\downarrow], \text{Im}[\eta_\downarrow])$  are mapped to  $\mathbb{S}^2$  coordinates  $(S_x, S_y, S_z)$ , and  $p, q$  are integers prime to each other. The Hopf invariant for the map  $f$  is known to be  $\chi(f) = \pm pq$  with the sign determined by the orientation of the three-sphere [57]. To construct physical Hamiltonians,  $\boldsymbol{\eta}$  can in turn be considered as another map  $g$  from the first Brillouin zone (BZ) to the three-sphere:  $\mathbb{T}^3 \rightarrow \mathbb{S}^3$

$$\begin{aligned} \eta_\uparrow(\mathbf{k}) &= \sin k_x + i \sin k_y, \\ \eta_\downarrow(\mathbf{k}) &= \sin k_z + i(\cos k_x + \cos k_y + \cos k_z + h), \end{aligned} \quad (2)$$

where  $\mathbb{T}^3$  is a 3D torus (describing the first BZ). Thus, the map  $\mathbf{S}(\mathbf{k}) = (S_x(\mathbf{k}), S_y(\mathbf{k}), S_z(\mathbf{k}))$  can be regarded as a composition of two maps,  $\mathbf{S} = f \circ g$ . In momentum space, we construct a tight-binding Hamiltonian based on  $\mathbf{S}(\mathbf{k})$  through  $H = \sum_{\mathbf{k}} \psi_{\mathbf{k}}^\dagger \mathcal{H}(\mathbf{k}) \psi_{\mathbf{k}}$  with  $\psi_{\mathbf{k}}^\dagger = (c_{\mathbf{k}\uparrow}^\dagger, c_{\mathbf{k}\downarrow}^\dagger)$  and

$$\mathcal{H}(\mathbf{k}) = \mathbf{S}(\mathbf{k}) \cdot \boldsymbol{\sigma}, \quad (3)$$

where  $c_{\mathbf{k}\uparrow}^\dagger, c_{\mathbf{k}\downarrow}^\dagger$  are fermionic creation operators and  $\boldsymbol{\sigma} = (\sigma^x, \sigma^y, \sigma^z)$  are three Pauli matrices. The Hamiltonian  $\mathcal{H}(\mathbf{k})$  contains  $(p+q)$ th order polynomials of  $\sin(\mathbf{k})$  and  $\cos(\mathbf{k})$ , which correspond to  $(p+q)$ -th neighbor hoppings in real space [38].

To study the topological properties of the Hamiltonian in Eq. (3), we define a normalized (pseudo-) spin field  $\hat{\mathbf{S}}(\mathbf{k}) = \mathbf{S}(\mathbf{k})/|\mathbf{S}(\mathbf{k})|$  (the normalization does not affect the topological properties). Hopf invariant, also known as Hopf charge or Hopf index, can be computed as an integral [37, 38]:

$$\chi(\hat{\mathbf{S}}) = - \int_{\text{BZ}} \mathbf{F} \cdot \mathbf{A} \, d^3\mathbf{k}, \quad (4)$$

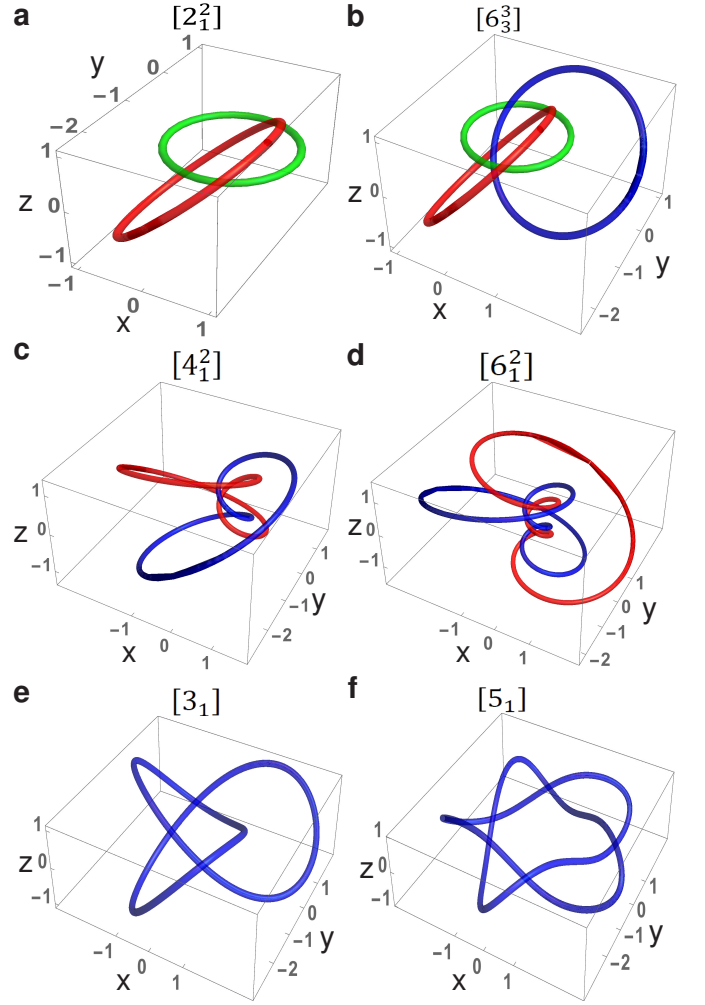


**FIG. 1. Knots and links hidden in Hopf insulators.** These knots and links correspond to preimages of three different spin orientations  $\hat{\mathbf{S}}_1 = (1, 0, 0)$ ,  $\hat{\mathbf{S}}_2 = (0, 1, 0)$  and  $\hat{\mathbf{S}}_3 = (0, 0, 1)$  living on  $\mathbb{S}^2$ . The loops in red (blue, green) are preimages of  $\hat{\mathbf{S}}_1$  ( $\hat{\mathbf{S}}_2$ ,  $\hat{\mathbf{S}}_3$ ) obtained from the contour plot  $f^{-1}(\hat{\mathbf{S}}_1)$  ( $f^{-1}(\hat{\mathbf{S}}_2)$ ,  $f^{-1}(\hat{\mathbf{S}}_3)$ ) in a stereographic coordinate system (see Methods section). The symbols inside each square bracket denote the standard Alexander–Briggs notation for the corresponding knot (link). The four links are: (a) the Hopf link, (b) the  $6_3^3$  link, (c) the Solomon’s link, and (d) the  $6_1^2$  link. The two knots are: (e) the trefoil knot and (f) the Solomon seal knot. The parameters are chosen as:  $p = q = 1$  in (a) and (b);  $p = 1, q = 2$  in (c);  $p = 1, q = 3$  in (d);  $p = 3, q = 2$  in (e) and  $p = 5, q = 2$  in (f).  $h = 2$  for (a–f). From (a–d), it is evident that the linking number of two different preimage contours is equal to the Hopf invariant  $\chi(f)$ .

where  $\mathbf{F}$  is the Berry curvature defined as  $F_\mu = \frac{1}{8\pi} \epsilon_{\mu\nu\tau} \hat{\mathbf{S}} \cdot (\partial_\nu \hat{\mathbf{S}} \times \partial_\tau \hat{\mathbf{S}})$  with  $\epsilon_{\mu\nu\tau}$  being the Levi-Civita symbol and  $\partial_{\nu,\tau} \equiv \partial_{k_{\nu,\tau}}$  ( $\mu, \nu, \tau \in \{x, y, z\}$ ), and  $\mathbf{A}$  is the associated Berry connection satisfying  $\nabla \times \mathbf{A} = \mathbf{F}$ . Direct calculations give  $\chi(\hat{\mathbf{S}}) = \pm pq$  if  $1 < |h| < 3$ ,  $\chi(\hat{\mathbf{S}}) = \pm 2pq$  if  $|h| < 1$ , and  $\chi(\hat{\mathbf{S}}) = 0$  otherwise [38]. This can be

understood intuitively by decomposing the composition map,  $\chi(\hat{\mathbf{S}}) = \chi(f)\Lambda(g) = \pm pq\Lambda(g)$ , where the map  $g$  is classified by another topological invariant

$$\Lambda(g) = \frac{1}{12\pi^2} \int_{\text{BZ}} d\mathbf{k} \epsilon_{\mu\nu\rho\tau} \frac{\epsilon_{\alpha\beta\gamma}}{|\boldsymbol{\eta}|^4} \eta_\mu \partial_\alpha \eta_\nu \partial_\beta \eta_\rho \partial_\gamma \eta_\tau. \quad (5)$$

With  $g$  given by Eq. (2), one obtains  $\Lambda(g) = 1$  if  $1 < |h| < 3$ ,  $\Lambda(g) = -2$  if  $|h| < 1$ , and  $\Lambda(g) = 0$  otherwise. Geometrically,  $\Lambda(g)$  counts how many times  $\mathbb{T}^3$  wraps around  $\mathbb{S}^3$  nontrivially under the map  $g$ , and  $\chi(f)$  describes how many times  $\mathbb{S}^3$  wraps around  $\mathbb{S}^2$  nontrivially under  $f$ . Their composition gives the Hopf invariant  $\chi(\hat{\mathbf{S}})$  [38].

The spin field  $\hat{\mathbf{S}}$  can be viewed as a map from  $\mathbb{T}^3$  to  $\mathbb{S}^2$ . While the domain  $\mathbb{T}^3$  is three-dimensional, the target space  $\mathbb{S}^2$  is two-dimensional. As a consequence, the preimage of a point in  $\mathbb{S}^2$  should be a closed loop in  $\mathbb{T}^3$ , and the linking number of two such loops corresponds to the Hopf invariant  $\chi(\hat{\mathbf{S}})$ . Similarly, the linking number of two preimage loops in  $\mathbb{S}^3$  under the map  $f$  gives the Hopf invariant  $\chi(f)$ , which is part of  $\chi(\hat{\mathbf{S}})$ . For easy visualization of knots and links, we work with  $\mathbb{S}^3$  rather than  $\mathbb{T}^3$  and probe the Hopf index  $\chi(f)$ . Fig. 1 shows several links and knots corresponding to certain spin orientations by using stereographic coordinates to represent  $\mathbb{S}^3$  (see Methods section). It is clear from the figure that the linking number of two preimage contours of distinct spin orientations is equal to the Hopf invariant  $\chi(f)$ . More interestingly, we note that even a single preimage contour may form a highly nontrivial knot when  $p$  and  $q$  become large. For instance, the trefoil knot and the Solomon seal knot plotted in Fig. 1e and Fig. 1f are two well-known nontrivial knots with nonunit knot polynomials [58]. More complex knots and links emerge for larger  $p$  and  $q$ .

A nonvanishing value of  $\chi(\hat{\mathbf{S}})$  also indicates that the spin field  $\hat{\mathbf{S}}$  has a nontrivial texture that cannot be continuously deformed into a trivial one. Mathematically, the Hopf invariant in Eq. (4) is a characteristic topological invariant of a sphere fiber bundle and a nonvanishing  $\chi$  generally precludes the existence of a global section due to the obstruction theory, in analogy to the scenario where nonzero Chern numbers forbid the tangent bundle of a two-sphere to have a global section [59]. A physical interpretation is that one can never untwist  $\hat{\mathbf{S}}$  smoothly unless a topological phase transition is crossed. In Fig. 2, the simplest nontrivial spin texture corresponding to  $\chi(f) = 1$  is sketched. One may regard  $\hat{\mathbf{S}}$  as a unit continuous vector field. In the stereographic coordinates,  $\hat{\mathbf{S}}$  resembles a nontrivial solution to the Faddeev-Skyrme model [39] with Hopf charge one. In this sense,  $\hat{\mathbf{S}}$  is a special realization of Hopfions, which are 3D topological solitons with broad applications but has hitherto escaped experimental observations [60]. In the next section, we will show that

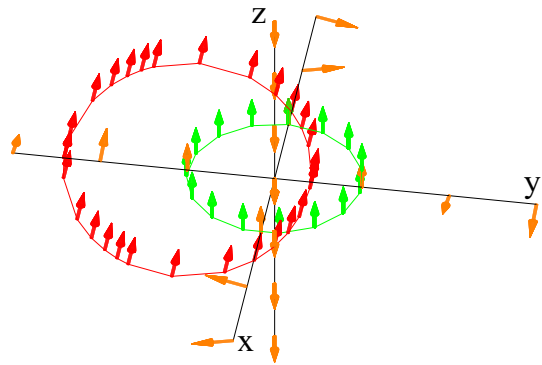


FIG. 2. **Knotted spin texture in stereographic coordinates.** We sketch out the spin orientations along each axis and on two circles. The parameters are chosen as  $p = q = 1$  and  $h = 2$ . Spins reside on the red (green) circle point to the  $x$  ( $z$ ) direction and those on the  $z$  axis all point to the south (negative  $z$  direction). Also, all spins faraway from the origin asymptotically point to the south. This spin texture is nontrivial (twisted with  $\chi(f) = 1$ ) and cannot be untwined continuously unless a topological phase transition is crossed.

all these nontrivial knots, links, and spin textures can be measured in cold-atom experiments with time-of-flight imaging.

**Probe knots and topology in optical lattices.** Hopf insulators are special topological insulators that have not been seen in solid systems. Although some magnetic compounds such as  $\text{R}_2\text{Mo}_2\text{O}_7$ , with R being a rare earth ion, are proposed to be possible candidates [37], actual realization of the Hopf insulator phase in solid remains very challenging due to the complicated spin-orbit couplings. The rapid experimental progress in synthetic spin-orbit couplings with cold atoms [40–47] provides a new promising platform to simulate various topological phases. Actually, some model Hamiltonians, which are initially proposed mainly for theoretical studies and thought to be out of reach for experiments due to their unusual and complex couplings, have indeed been realized in cold-atom labs. For instance, an experimental observation of the topological Haldane model with ultracold atoms has been achieved recently [46]. It is likely that Hopf insulators will also have a cold-atom experimental implementation in the near future. With this in mind, we illustrate below how to detect the Hopf invariant and probe the knot structure with ultracold atoms in optical lattices assuming a Hopf Hamiltonian is realized. In Ref. [61], we introduced a generic method to directly measure various topological invariants based on time-of-flight imaging of cold atoms. This method is applicable to the detection of topological band insulators in any spatial dimensions. Here we apply it to the detection of Hopf insulators in cold-atom systems.

From Eq. (4), to extract the Hopf invariant, it is essen-

TABLE I. **Hopf index extracted from simulated time-of-flight images.** Simulated experimental results for Hopf invariants with different lattice sizes and varying  $h$ . Four different situations, one with periodic and three with open boundary conditions, are considered. The Hopf index can be found from the momentum density distributions obtained directly through time-of-flight imaging. The parameters used are  $p = q = 1$  and  $\gamma_t = \gamma_r = 0.1$ .

$h$	Size	Periodic	Open	Trap	Pert.+Trap
0	$10^3$	-2.058	-1.956	-1.985	-1.986
0	$20^3$	-2.019	-2.019	-2.025	-2.025
2	$10^3$	1.041	0.982	0.986	0.986
2	$20^3$	1.012	1.008	1.009	1.009
4	$20^3$	$-9.6 \times 10^{-5}$	$2.9 \times 10^{-5}$	$6.6 \times 10^{-5}$	$6.7 \times 10^{-5}$

tial to obtain the spin texture  $\hat{\mathbf{S}}(\mathbf{k})$  in momentum space. In experiment, one discretizes the BZ and a pixelized version of  $\hat{\mathbf{S}}(\mathbf{k})$  can be obtained through time-of-flight imaging. Refs [61, 62] describe in detail how to measure  $\hat{\mathbf{S}}(\mathbf{k})$  in experiment. One astute observation [62] was that the spin component is related to the density distributions as  $\hat{S}_z(\mathbf{k}) = [n_\uparrow(\mathbf{k}) - n_\downarrow(\mathbf{k})]/[n_\uparrow(\mathbf{k}) + n_\downarrow(\mathbf{k})]$ . A fast Raman or radio frequency pulse before time-of-flight rotates the atomic states and maps  $\hat{S}_x$  and  $\hat{S}_y$  to  $\hat{S}_z$ , enabling one to reconstruct the whole pixelized  $\hat{\mathbf{S}}(\mathbf{k})$ . To obtain the 3D momentum distributions, one may map out the 2D densities  $n(k_x, k_y, k_{z_i})$  with various  $k_{z_i}$  layers [61]. It is encouraging to see in Table I that ten or twenty layers are sufficient to produce very good results.

With the measured  $\hat{\mathbf{S}}(\mathbf{k})$  in hand, we can extract the Hopf index directly. As  $F_\mu = \frac{1}{8\pi} \epsilon_{\mu\nu\tau} \hat{\mathbf{S}} \cdot (\partial_\nu \hat{\mathbf{S}} \times \partial_\tau \hat{\mathbf{S}})$ , we obtain the Berry curvature  $\mathbf{F}$  at each pixel of the BZ. We then find the Berry connection by solving a discrete version of the equation  $\nabla \times \mathbf{A} = \mathbf{F}$  in the Coulomb gauge  $\nabla \cdot \mathbf{A} = 0$ . Hopf index can thus be extracted from Eq. (4), replacing the integral by a discrete summation. To simulate real experiments, we write down the Hamiltonian  $H$  in real space and consider a finite-size lattice with open boundaries. In addition, we add two terms into the Hamiltonian to account for typical experimental imperfections. The first one is a global harmonic trap parametrized by  $\gamma_t$ , and the second one is a random noise characterized by  $\gamma_r$  (see Methods section). For the simplest case of  $p = q = 1$ , we numerically diagonalize the realistic real-space Hamiltonian and compute the corresponding Hopf index for different  $h$  based on the method introduced in Ref. [61]. Our results are summarized in Table I. We can see that the Hopf index converges rapidly to the expected value as the lattice size increases and the detection method remains robust against typical experimental imperfections.

As discussed in the previous section, a nonvanishing  $\chi(\hat{\mathbf{S}})$  implies a nontrivial spin texture. With cold atoms, one can actually visualize this nontrivial spin texture

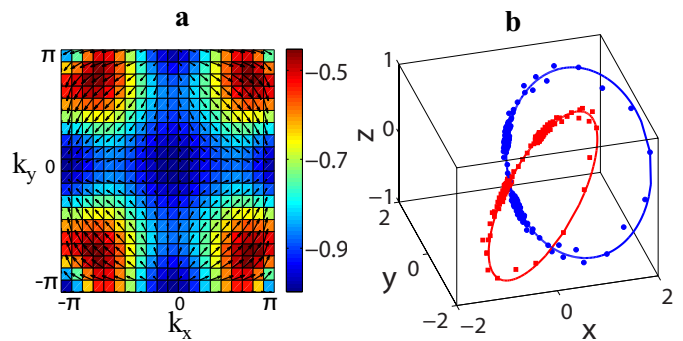


FIG. 3. **Spin texture and the Hopf link from numerical simulations of real experiments.** (a) Simulated spin texture in the  $k_x$ - $k_y$  plane with  $k_z = 0$ . The background color scale shows the magnitude of the out-of-plane component  $\hat{S}_z$ , and the arrows show the magnitude and direction of spins in the  $k_x$ - $k_y$  plane. (b) Simulated Hopf link with linking number one. The red (blue) circle represents the theoretical preimage of  $\hat{\mathbf{S}}_1$  ( $\hat{\mathbf{S}}_2$ ) and the scattered red squares (blue dots) are numerically simulated preimages of the  $\epsilon$ -neighborhood of  $\hat{\mathbf{S}}_1$  ( $\hat{\mathbf{S}}_2$ ) (see Methods section), which can be observed from time-of-flight images. The spin texture and preimages are computed by exactly diagonalizing the real space Hamiltonian with a lattice size  $40 \times 40 \times 40$  under an open boundary condition. The parameters are chosen as  $p = q = 1$ ,  $h = 2$ ,  $\gamma_t = 0.01$ ,  $\gamma_r = 0.01$ , and  $\epsilon = 0.15$ .

in the momentum space. In Fig. 3a, we plot a slice of the observed  $\hat{\mathbf{S}}(\mathbf{k})$  with  $k_z = 0$ . Although this 2D plot cannot display full information of the 3D spin texture, its twisted spin orientations do offer a glimpse of the whole nontrivial structure. It is worthwhile to note that this texture is distinct from typical 2D skyrmion [63] configurations, wherein swirling structure is a prominent feature [64, 65]. More slices can be mapped out from the experiment to look for traits of a Hopfion. With  $\hat{\mathbf{S}}(\mathbf{k})$ , one may also explicitly see knots and links in experiment. In the ideal case and continuum limit, the preimages of two different orientations of  $\hat{\mathbf{S}}(\mathbf{k})$  should be linked with a linking number equal to the Hopf index. Hence, if we map out these preimages, we would obtain a link. However, a real experiment always involves various kinds of noises. As a result, the measured  $\hat{\mathbf{S}}(\mathbf{k})$  cannot be perfectly accurate. Moreover, due to the finite size, the observed  $\hat{\mathbf{S}}(\mathbf{k})$  is discrete and only has a finite resolution. To circumvent these difficulties, we keep track of the preimages of a small neighborhood of the chosen orientations (see Methods section). We plotted a Hopf link in Fig. 3b based on the numerically simulated experimental results. From this figure and many other numerical simulations (not shown here for conciseness), we find that this link is stable against experimental imperfections. Varying  $h$  and other parameters characterizing the strength of noise change the shape of each circle, but the linked structure persists with linking number one.

## Discussion

Hopf insulators are a special class of topological insulators beyond the periodic table for topological insulators and superconductors [53, 54]. Their physical realization is of great importance but also especially challenging. With ultracold atoms in optical lattices, Hopf insulators could be realized using the Raman-assisted hopping technique [66–69]. The basic idea is analogous to that in Ref. [70], where a cold-atom implementation of 3D chiral topological insulators was proposed. Here we focus on how to measure the Hopf invariant and probe various intriguing knots and links, leaving a possible implementation protocol to the Supplementary Information. Other simpler experimental scenario for realizing Hopf insulators with cold atoms might also exist. A promising alternative is to consider periodically driven quantum systems, where modulation schemes can be tailored to implement diverse gauge fields [71] and an experimental realization of the Haldane model has been reported [46].

Hopf insulators provide a new platform for exploring the deep connection and interplay between knot theory and topological phenomena, on which our knowledge still remain limited. For instance, in the above discussions, we showed that many different kinds of knots and links are hidden in Hopf insulators. However, a complete list of such knots and links is still lacking and requires further investigations. These studies will reveal new fundamental physical principle, and in the same time, can offer new guiding principles for experimental studies. From Fig. 1, it seems that partial information of certain spin orientations is already sufficient to characterize the topology of the Hopf insulators. This observation may help simplify the experimental detections. Taking the case in Fig. 1e as an example, to determine whether the system has a nontrivial topology or not, we only need to do the time-of-flight measurements in the  $\hat{S}_y$  (or equivalently  $\hat{S}_z$ ) basis. Thus, no rotation induced by fast Raman or radio frequency pulses is needed. In the future, it would be interesting to explore potential applications of the knotted spin texture in designing spin devices based on topological states, which may have applications in spintronics and quantum information technologies [72].

In summary, we have shown that Hopf insulators support rich and highly nontrivial knot and link structures. We also demonstrated, via numerical simulations, that these exotic knots and associated nontrivial spin textures, which are robust to typical experimental imperfections, can be probed through time-of-flight imaging in cold atoms. Our results shed new light on the studies of topological insulators and open up a possibility to probe exotic knots and links in the cold-atom experimental platform.

## Methods

**Stereographic coordinates.** For Hopf insulators in a cubic

lattice, the first BZ is a 3D torus  $\mathbb{T}^3$ . Since it is not convenient to draw and visualize different knots and links in  $\mathbb{T}^3$ , we first do a map  $g$  to go from  $\mathbb{T}^3$  to  $\mathbb{S}^3$  and use a stereographic coordinate system to represent  $\mathbb{S}^3$ . The stereographic projection used in this paper is defined as:

$$(x, y, z) = \frac{1}{1 + \eta_4}(\eta_1, \eta_2, \eta_3), \quad (6)$$

where  $(x, y, z)$  and  $(\eta_1, \eta_2, \eta_3, \eta_4)$  are points of  $\mathbb{R}^3$  and  $\mathbb{S}^3$ , respectively.

**Perturbations to the Hamiltonian.** In realistic experiments, there are additional noises other than the ideal Hamiltonian given by Eq. (3). The first one is a weak global harmonic trap typically present in cold-atom experiment. It is of the form  $H_{\text{trap}} = \frac{1}{2}m\omega^2 \sum_{\mathbf{r}, \sigma} d_{\mathbf{r}}^2 c_{\mathbf{r}, \sigma}^\dagger c_{\mathbf{r}, \sigma}$ , where  $\sigma = \uparrow, \downarrow$ ,  $m$  is the mass of the atom and  $d_{\mathbf{r}}$  is the distance from the center of the trap to the lattice site  $\mathbf{r}$ . We use  $\gamma_t = m\omega^2 a^2/2$  to parametrize the relative strength of the trap with  $a$  denoting the lattice constant. The other perturbation we consider is a random noise of the form  $H_{\text{rand}} = \gamma_r \sum_{\mathbf{r}, \mathbf{r}', \sigma, \sigma'} c_{\mathbf{r}, \sigma}^\dagger \mathcal{R}_{\mathbf{r}\sigma, \mathbf{r}'\sigma'} c_{\mathbf{r}', \sigma'}$  where  $\gamma_r$  characterizes the strength of the noise and  $\mathcal{R}$  is a random Hermitian matrix with its largest eigenvalue normalized to unity.

## Seeing links and knots from the time-of-flight data.

As discussed in the main text, the spin orientation  $\hat{\mathbf{S}}(\mathbf{k})$  in real experiment is always pixelized with a finite resolution. Therefore, for a specific orientation,  $\hat{\mathbf{S}}_1$  for instance, the measured  $\hat{\mathbf{S}}(\mathbf{k})$  can only be approximately rather than exactly equal to  $\hat{\mathbf{S}}_1$  at any momentum point  $\mathbf{k}$ . Consequently, one need to consider a small  $\epsilon$ -neighborhood of  $\hat{\mathbf{S}}_1$ :

$$N_\epsilon(\hat{\mathbf{S}}_1) = \{\hat{\mathbf{S}} : |\hat{\mathbf{S}} - \hat{\mathbf{S}}_1| \leq \epsilon\}, \quad (7)$$

where  $|\hat{\mathbf{S}} - \hat{\mathbf{S}}_1| = [(\hat{S}_x - \hat{S}_{1x})^2 + (\hat{S}_y - \hat{S}_{1y})^2 + (\hat{S}_z - \hat{S}_{1z})^2]^{1/2}$  measures the distance between  $\hat{\mathbf{S}}$  and  $\hat{\mathbf{S}}_1$ . Let us denote the preimages of all orientations in  $N_\epsilon(\hat{\mathbf{S}}_1)$  as a set  $P_\epsilon(\hat{\mathbf{S}}_1) = (f \circ g)^{-1}[N_\epsilon(\hat{\mathbf{S}}_1)]$ . With a finite resolution, the BZ is discrete and contains finite momentum points, and so does  $P_\epsilon(\hat{\mathbf{S}}_1)$ . As a result, one should wisely choose an appropriate value for  $\epsilon$  so that  $P_\epsilon(\hat{\mathbf{S}}_1)$  contains a proper amount of momentum points to depict the loop structure of  $(f \circ g)^{-1}(\hat{\mathbf{S}}_1)$ . To obtain Fig. 3b in our numerical simulation, we examine the discrete  $\hat{\mathbf{S}}(\mathbf{k})$  (observed from time-of-flight measurements) at each momentum point  $\mathbf{k}$  and append  $\mathbf{k}$  into the set  $P_{1\epsilon}$  ( $P_{2\epsilon}$ ) if  $\hat{\mathbf{S}}(\mathbf{k})$  is in a  $\epsilon$ -neighborhood of  $\hat{\mathbf{S}}_1$  ( $\hat{\mathbf{S}}_2$ ). Then Fig. 3b can be obtained by plotting  $g(P_{1\epsilon})$  and  $g(P_{2\epsilon})$  in the stereographic coordinate system defined above.

## Acknowledgement

We thank X.-J. Liu, G. Ortiz, J. E. Moore, H. Zhai, and D. Thurston for helpful discussions. D.L.D., S.T.W. and L.M.D. are supported by the ARL, the IARPA LogiQ program, and the AFOSR MURI program, and acknowledge support from Tsinghua University for their visits. K.S. acknowledges support from NSF under Grant No. PHY1402971. D.L.D. is also supported by JQI-NSF-PFC and LPS-MPO-CMTC at the final stage of this paper.

## Author contributions

L.M.D. supervised the project. All authors conceived the idea, analysed and discussed the results. D.L.D. performed

the numerical simulations. All authors contributed to the writing of the manuscript.

## Additional Information

**Supplementary Information** accompanies this paper on:

**Competing financial interests:** The authors declare no competing financial interests.

- 
- [1] Kelvin, L. On vortex atoms. In *Proc. R. Soc. Edin.*, vol. 6, 94–105 (1867).
- [2] Bates, A. D., Maxwell, A. & Press, O. *DNA topology* (Oxford Univ. Press, Oxford, ed. 2, 2005, 2005).
- [3] Meluzzi, D., Smith, D. E. & Arya, G. Biophysics of knotting. *Annu. Rev. Biophys.* **39**, 349–366 (2010).
- [4] Chichak, K. S. *et al.* Molecular borromean rings. *Science* **304**, 1308–1312 (2004).
- [5] Han, D., Pal, S., Liu, Y. & Yan, H. Folding and cutting dna into reconfigurable topological nanostructures. *Nat. Nanotechnol.* **5**, 712–717 (2010).
- [6] Ponnuswamy, N., Cougnon, F. B., Clough, J. M., Pantoş, G. D. & Sanders, J. K. Discovery of an organic trefoil knot. *Science* **338**, 783–785 (2012).
- [7] de Gennes, P. G. *Scaling concepts in polymer physics* (Cornell Univ. Press, New York, 1979, 1979).
- [8] Faddeev, L. & Niemi, A. J. Stable knot-like structures in classical field theory. *Nature* **387**, 58–61 (1997).
- [9] Kedia, H., Bialynicki-Birula, I., Peralta-Salas, D. & Irvine, W. T. M. Tying knots in light fields. *Phys. Rev. Lett.* **111**, 150404 (2013).
- [10] Ricca, R. L., Samuels, D. C. & Barenghi, C. F. Evolution of vortex knots. *J. Fluid Mech.* **391**, 29–44 (1999).
- [11] Woltjer, L. A theorem on force-free magnetic fields. *Proc. Natl. Acad. Sci.* **44**, 489 (1958).
- [12] Kawaguchi, Y., Nitta, M. & Ueda, M. Knots in a spinor bose-einstein condensate. *Phys. Rev. Lett.* **100**, 180403 (2008).
- [13] Machon, T. & Alexander, G. P. Knots and nonorientable surfaces in chiral nematics. *Proceedings of the National Academy of Sciences* **110**, 14174–14179 (2013).
- [14] Machon, T. & Alexander, G. P. Knotted defects in nematic liquid crystals. *Phys. Rev. Lett.* **113**, 027801 (2014).
- [15] Alexander, G. P., Chen, B. G.-g., Matsumoto, E. A. & Kamien, R. D. Colloquium: Disclination loops, point defects, and all that in nematic liquid crystals. *Rev. Mod. Phys.* **84**, 497–514 (2012).
- [16] Buniy, R. V. & Kephart, T. W. A model of glueballs. *Phys. Rev. Lett.* **576**, 127–134 (2003).
- [17] Witten, E. Quantum field theory and the jones polynomial. *Commun. Math. Phys.* **121**, 351–399 (1989).
- [18] Senyuk, B. *et al.* Topological colloids. *Nature* **493**, 200–205 (2013).
- [19] Tkalec, U., Ravnik, M., Čopar, S., Žumer, S. & Muševič, I. Reconfigurable knots and links in chiral nematic colloids. *Science* **333**, 62–65 (2011).
- [20] Chen, B. G.-g., Ackerman, P. J., Alexander, G. P., Kamien, R. D. & Smalyukh, I. I. Generating the hopf fibration experimentally in nematic liquid crystals. *Phys. Rev. Lett.* **110**, 237801 (2013).
- [21] Martinez, A. *et al.* Mutually tangled colloidal knots and induced defect loops in nematic fields. *Nature materials* (2014).
- [22] Dennis, M. R., King, R. P., Jack, B., O’Holleran, K. & Padgett, M. J. Isolated optical vortex knots. *Nat. Phys.* **6**, 118–121 (2010).
- [23] Kleckner, D. & Irvine, W. T. Creation and dynamics of knotted vortices. *Nat. Phys.* **9**, 253–258 (2013).
- [24] Irvine, W. T. & Kleckner, D. Liquid crystals: Tangled loops and knots. *Nature materials* **13**, 229–231 (2014).
- [25] Hall, D. S. *et al.* Tying quantum knots. *Nat. Phys.* **12**, 478–483 (2016).
- [26] Berezinskii, V. Destruction of long-range order in one-dimensional and two-dimensional systems having a continuous symmetry group i. classical systems. *Soviet Journal of Experimental and Theoretical Physics* **32**, 493 (1971).
- [27] Kosterlitz, J. M. & Thouless, D. J. Ordering, metastability and phase transitions in two-dimensional systems. *Journal of Physics C: Solid State Physics* **6**, 1181 (1973).
- [28] Cage, M. E. *et al.* *The quantum Hall effect* (Springer Science & Business Media, 2012).
- [29] Qi, X.-L. & Zhang, S.-C. Topological insulators and superconductors. *Rev. Mod. Phys.* **83**, 1057–1110 (2011).
- [30] Hasan, M. Z. & Kane, C. L. Colloquium: Topological insulators. *Rev. Mod. Phys.* **82**, 3045–3067 (2010).
- [31] Moore, J. E. The birth of topological insulators. *Nature* **464**, 194–198 (2010).
- [32] Chen, X., Gu, Z.-C., Liu, Z.-X. & Wen, X.-G. Symmetry-protected topological orders in interacting bosonic systems. *Science* **338**, 1604–1606 (2012).
- [33] Thouless, D. J., Kohmoto, M., Nightingale, M. P. & den Nijs, M. Quantized hall conductance in a two-dimensional periodic potential. *Phys. Rev. Lett.* **49**, 405–408 (1982).
- [34] Qi, X.-L., Li, R., Zang, J. & Zhang, S.-C. Inducing a magnetic monopole with topological surface states. *Science* **323**, 1184–1187 (2009).
- [35] Rosenberg, G., Guo, H.-M. & Franz, M. Wormhole effect in a strong topological insulator. *Phys. Rev. B* **82**, 041104 (2010).
- [36] Rosenberg, G. & Franz, M. Witten effect in a crystalline topological insulator. *Phys. Rev. B* **82**, 035105 (2010).
- [37] Moore, J. E., Ran, Y. & Wen, X.-G. Topological surface states in three-dimensional magnetic insulators. *Phys. Rev. Lett.* **101**, 186805 (2008).
- [38] Deng, D.-L., Wang, S.-T., Shen, C. & Duan, L.-M. Hopf insulators and their topologically protected surface states. *Phys. Rev. B* **88**, 201105 (2013).
- [39] Faddeev, L. Quantization of solitons. *Princeton preprint IAS-75-QS70* (1975).
- [40] Lin, Y.-J., Jimenez-Garcia, K. & Spielman, I. Spin-orbit-coupled bose-einstein condensates. *Nature* **471**, 83–86 (2011).
- [41] Galitski, V. & Spielman, I. B. Spin-orbit coupling in quantum gases. *Nature* **494**, 49–54 (2013).
- [42] Beeler, M. *et al.* The spin hall effect in a quantum gas. *Nature* (2013).
- [43] Dalibard, J., Gerbier, F., Juzeliūnas, G. & Öhberg, P. Colloquium: Artificial gauge potentials for neutral atoms. *Rev. Mod. Phys.* **83**, 1523–1543 (2011).
- [44] Bloch, I., Dalibard, J. & Nascimbène, S. Quantum simulations with ultracold quantum gases. *Nat. Phys.* **8**, 267–276 (2012).
- [45] Goldman, N., Budich, J. & Zoller, P. Topological quan-

- tum matter with ultracold gases in optical lattices. *Nat. Phys.* **12**, 639–645 (2016).
- [46] Jotzu, G. *et al.* Experimental realization of the topological haldane model with ultracold fermions. *Nature* **515**, 237–240 (2014).
- [47] Wu, Z. *et al.* Realization of two-dimensional spin-orbit coupling for bose-einstein condensates. *Science* **354**, 83–88 (2016).
- [48] Fu, L., Kane, C. L. & Mele, E. J. Topological insulators in three dimensions. *Phys. Rev. Lett.* **98**, 106803 (2007).
- [49] Moore, J. E. & Balents, L. Topological invariants of time-reversal-invariant band structures. *Phys. Rev. B* **75**, 121306 (2007).
- [50] Roy, R. Topological phases and the quantum spin hall effect in three dimensions. *Phys. Rev. B* **79**, 195322 (2009).
- [51] Hsieh, D. *et al.* A topological dirac insulator in a quantum spin hall phase. *Nature* **452**, 970–974 (2008).
- [52] Xia, Y. *et al.* Observation of a large-gap topological-insulator class with a single dirac cone on the surface. *Nat. Phys.* **5**, 398–402 (2009).
- [53] Schnyder, A. P., Ryu, S., Furusaki, A. & Ludwig, A. W. W. Classification of topological insulators and superconductors in three spatial dimensions. *Phys. Rev. B* **78**, 195125 (2008).
- [54] Kitaev, A. Periodic table for topological insulators and superconductors. *AIP Conf. Proc.* **1134**, 22 (2009).
- [55] Chang, C.-Z. *et al.* Experimental observation of the quantum anomalous hall effect in a magnetic topological insulator. *Science* **340**, 167–170 (2013).
- [56] Deng, D.-L., Wang, S.-T. & Duan, L.-M. Systematic construction of tight-binding hamiltonians for topological insulators and superconductors. *Phys. Rev. B* **89**, 075126 (2014).
- [57] Whitehead, J. H. An expression of hopf’s invariant as an integral. *Proc. Nat. Acad. Sci.* **33**, 117 (1947).
- [58] Kauffman, L. H. *Knots and physics*, vol. 53 (World scientific, 2013).
- [59] Hatcher, A. *Algebraic Topology* (Cambridge University Press, 2002).
- [60] Hietarinta, J., Palmu, J., Jäykkä, J. & Pakkanen, P. Scattering of knotted vortices (hopfions) in the faddeev–skyrme model. *New J. Phys.* **14**, 013013 (2012).
- [61] Deng, D.-L., Wang, S.-T. & Duan, L.-M. Direct probe of topological order for cold atoms. *Phys. Rev. A* **90**, 041601 (2014).
- [62] Alba, E., Fernandez-Gonzalvo, X., Mur-Petit, J., Pachos, J. K. & Garcia-Ripoll, J. J. Seeing topological order in time-of-flight measurements. *Phys. Rev. Lett.* **107**, 235301 (2011).
- [63] Skyrme, T. H. R. A unified field theory of mesons and baryons. *Nucl. Phys.* **31**, 556–569 (1962).
- [64] Yu, X. *et al.* Real-space observation of a two-dimensional skyrmion crystal. *Nature* **465**, 901–904 (2010).
- [65] Röbler, U., Bogdanov, A. & Pfleiderer, C. Spontaneous skyrmion ground states in magnetic metals. *Nature* **442**, 797–801 (2006).
- [66] Jaksch, D. & Zoller, P. Creation of effective magnetic fields in optical lattices: the hofstadter butterfly for cold neutral atoms. *New J. Phys.* **5**, 56 (2003).
- [67] Miyake, H., Siviloglou, G. A., Kennedy, C. J., Burton, W. C. & Ketterle, W. Realizing the harper hamiltonian with laser-assisted tunneling in optical lattices. *Phys. Rev. Lett.* **111**, 185302 (2013).
- [68] Aidelsburger, M. *et al.* Realization of the hofstadter hamiltonian with ultracold atoms in optical lattices. *Phys. Rev. Lett.* **111**, 185301 (2013).
- [69] Aidelsburger, M. *et al.* Experimental realization of strong effective magnetic fields in an optical lattice. *Phys. Rev. Lett.* **107**, 255301 (2011).
- [70] Wang, S.-T., Deng, D.-L. & Duan, L.-M. Probe of three-dimensional chiral topological insulators in an optical lattice. *Phys. Rev. Lett.* **113**, 033002 (2014).
- [71] Goldman, N. & Dalibard, J. Periodically driven quantum systems: Effective hamiltonians and engineered gauge fields. *Phys. Rev. X* **4**, 031027 (2014).
- [72] Jungwirth, T. *et al.* Spin-dependent phenomena and device concepts explored in (Ga,Mn)As. *Rev. Mod. Phys.* **86**, 855–896 (2014).

## Supplementary Information: Probe knots and Hopf insulators with ultracold atoms

In the main text, we have been focused on how to measure the Hopf invariant and probe knots and links using the standard time-of-flight imaging techniques. In this Supplementary Information, we propose a possible experimental scheme to realize Hopf insulators with ultracold atoms in optical lattices. For simplicity, we consider the case of  $p = q = 1$ . After a Fourier transform, the corresponding Hamiltonian in real space reads  $H = H_{\text{sf}} + H_{\text{sp}}$ , where  $H_{\text{sf}}$  denotes the collection of all terms with spin flips:

$$\begin{aligned} H_{\text{sf}} = & \sum_{\mathbf{r}} \frac{1}{2} [c_{\mathbf{r},\uparrow}^\dagger c_{\mathbf{r}+2\hat{x},\downarrow} - c_{\mathbf{r},\uparrow}^\dagger c_{\mathbf{r}-2\hat{x},\downarrow} - (1-i)c_{\mathbf{r},\uparrow}^\dagger c_{\mathbf{r}-\hat{x}-\hat{y},\downarrow} + (1+i)c_{\mathbf{r},\uparrow}^\dagger c_{\mathbf{r}+\hat{x}-\hat{y},\downarrow} - (1+i)c_{\mathbf{r},\uparrow}^\dagger c_{\mathbf{r}-\hat{x}+\hat{y},\downarrow} + ic_{\mathbf{r},\uparrow}^\dagger c_{\mathbf{r}-2\hat{y},\downarrow} \\ & + (1-i)c_{\mathbf{r},\uparrow}^\dagger c_{\mathbf{r}+\hat{x}+\hat{y},\downarrow} - ic_{\mathbf{r},\uparrow}^\dagger c_{\mathbf{r}+2\hat{y},\downarrow} - 2c_{\mathbf{r},\uparrow}^\dagger c_{\mathbf{r}-\hat{x}-\hat{z},\downarrow} + 2c_{\mathbf{r},\uparrow}^\dagger c_{\mathbf{r}+\hat{x}-\hat{z},\downarrow} + 2ic_{\mathbf{r},\uparrow}^\dagger c_{\mathbf{r}-\hat{y}-\hat{z},\downarrow} - 2ic_{\mathbf{r},\uparrow}^\dagger c_{\mathbf{r}+\hat{y}-\hat{z},\downarrow} \\ & + 2h(c_{\mathbf{r},\uparrow}^\dagger c_{\mathbf{r}+\hat{x},\downarrow} - c_{\mathbf{r},\uparrow}^\dagger c_{\mathbf{r}-\hat{x},\downarrow} + ic_{\mathbf{r},\uparrow}^\dagger c_{\mathbf{r}-\hat{y},\downarrow} - ic_{\mathbf{r},\uparrow}^\dagger c_{\mathbf{r}+\hat{y},\downarrow})] + \text{h.c.}, \end{aligned}$$

and  $H_{\text{sp}}$  denotes the collection of all other terms:

$$\begin{aligned} H_{\text{sp}} = & \sum_{\mathbf{r}} \frac{1}{2} [c_{\mathbf{r},\downarrow}^\dagger c_{\mathbf{r}-2\hat{x},\downarrow} + c_{\mathbf{r},\downarrow}^\dagger c_{\mathbf{r}+2\hat{x},\downarrow} + c_{\mathbf{r},\downarrow}^\dagger c_{\mathbf{r}+\hat{x}+\hat{y},\downarrow} + c_{\mathbf{r},\downarrow}^\dagger c_{\mathbf{r}-\hat{x}-\hat{y},\downarrow} + c_{\mathbf{r},\downarrow}^\dagger c_{\mathbf{r}-\hat{x}+\hat{y},\downarrow} + c_{\mathbf{r},\downarrow}^\dagger c_{\mathbf{r}+\hat{x}-\hat{y},\downarrow} + c_{\mathbf{r},\downarrow}^\dagger c_{\mathbf{r}-2\hat{y},\downarrow} \\ & + c_{\mathbf{r},\downarrow}^\dagger c_{\mathbf{r}+2\hat{y},\downarrow} + c_{\mathbf{r},\downarrow}^\dagger c_{\mathbf{r}+\hat{x}+\hat{z},\downarrow} + c_{\mathbf{r},\downarrow}^\dagger c_{\mathbf{r}-\hat{x}-\hat{z},\downarrow} + c_{\mathbf{r},\downarrow}^\dagger c_{\mathbf{r}-\hat{x}+\hat{z},\downarrow} + c_{\mathbf{r},\downarrow}^\dagger c_{\mathbf{r}+\hat{x}-\hat{z},\downarrow} + c_{\mathbf{r},\downarrow}^\dagger c_{\mathbf{r}+\hat{y}+\hat{z},\downarrow} + c_{\mathbf{r},\downarrow}^\dagger c_{\mathbf{r}-\hat{y}-\hat{z},\downarrow} \\ & + c_{\mathbf{r},\downarrow}^\dagger c_{\mathbf{r}-\hat{y}+\hat{z},\downarrow} + c_{\mathbf{r},\downarrow}^\dagger c_{\mathbf{r}+\hat{y}-\hat{z},\downarrow} + 2h(c_{\mathbf{r},\downarrow}^\dagger c_{\mathbf{r}+\hat{x},\downarrow} + c_{\mathbf{r},\downarrow}^\dagger c_{\mathbf{r}-\hat{x},\downarrow} + c_{\mathbf{r},\downarrow}^\dagger c_{\mathbf{r}+\hat{y},\downarrow} + c_{\mathbf{r},\downarrow}^\dagger c_{\mathbf{r}-\hat{y},\downarrow} \\ & + c_{\mathbf{r},\downarrow}^\dagger c_{\mathbf{r}+\hat{z},\downarrow} + c_{\mathbf{r},\downarrow}^\dagger c_{\mathbf{r}-\hat{z},\downarrow}) + 2(1+h^2)c_{\mathbf{r},\downarrow}^\dagger c_{\mathbf{r},\downarrow}] - [|\downarrow \rightarrow \uparrow]. \end{aligned}$$

To realize Hopf insulators with ultracold atoms, the method used here is similar to that in Ref. [70], where a cold-atom implementation of three-dimensional (3D) chiral topological insulators was proposed. We consider cold fermionic atoms ( $^6\text{Li}$  for example) in a 3D cubic optical lattice and choose two internal atomic levels (hyperfine states) as our spin states  $|\uparrow\rangle$  and  $|\downarrow\rangle$ . Other levels are initially depopulated by optical pumping and transitions to those levels are forbidden due to a large energy detuning or carefully selected laser polarizations. In real space, the Hamiltonian has spin-orbit coupled hoppings along nine possible directions. Here, we explicitly demonstrate how to engineer the specific hoppings along the  $\mathbf{v} = \hat{x} + \hat{y}$  direction. For other directions, the realization scheme will be similar and thus omitted for conciseness. The hopping terms in the  $\mathbf{v}$  direction can be written as

$$H_{\mathbf{v}} = \frac{1}{2} \sum_{\mathbf{r}} [-(1+i)c_{\mathbf{r},\downarrow}^\dagger - c_{\mathbf{r},\uparrow}^\dagger] c_{\mathbf{r}+\mathbf{v},\uparrow} + [(1-i)c_{\mathbf{r},\uparrow}^\dagger + c_{\mathbf{r},\downarrow}^\dagger] c_{\mathbf{r}+\mathbf{v},\downarrow} + \text{h.c.} \quad (\text{S1})$$

Apparently,  $H_{\mathbf{v}}$  consists of various hopping terms coupled with spin rotations. Basically, both spin  $|\uparrow\rangle$  and  $|\downarrow\rangle$  hop along the  $-\mathbf{v}$  direction to become a superposition of both spin states. We can decompose the four different hopping terms and each of them can be achieved via Raman-assisted tunnelings [66–68]. For instance, the first two hoppings can be activated by two Raman pairs,  $\Omega_{\uparrow}$ ,  $\tilde{\Omega}_{1\mathbf{v}}$ , and  $\Omega_{\downarrow}$ ,  $\Omega_{1\mathbf{v}}$ , where  $\Omega_{\uparrow}$  is in common;  $\tilde{\Omega}_{1\mathbf{v}}$  and  $\Omega_{1\mathbf{v}}$  can be drawn from the same beam split by an electric or acoustic optical modulator. The phase and strength of the hopping can be controlled by the laser phase and intensity (see caption of Fig. S1). Similarly, the other two hopping terms can be triggered by the Raman triplet  $\Omega_{2\mathbf{v}}$ ,  $\Omega_{2\mathbf{v}}$  and  $\Omega_{\downarrow}$  as shown in Fig. S1.

One may notice that the parity (left-right) symmetry is explicitly broken and natural hoppings are suppressed. Both of these can be achieved by a homogeneous energy gradient along the  $\mathbf{v}$  direction, which can be accomplished, for instance, by the magnetic field gradient, dc- or ac-Stark shift gradient, or the natural gravitational field [67, 68, 70]. We denote the linear energy shift per site in the  $\mathbf{v}$  direction by  $\Delta_{\mathbf{v}}$  and impose that natural tunneling rate  $t_0 \ll \Delta_{\mathbf{v}}$ . As a consequence, the natural tunneling probability  $(t_0/\Delta_{\mathbf{v}})^2$  is negligible in this tilted lattice. The energy offset also forbids Raman-assisted tunnelings in the opposite direction other than the ones prescribed above. Incommensurate tilts along different directions also suppress unwanted couplings among them. The detuning  $\delta_1$  and  $\delta_2$  for the two Raman triplets should also be different, so that no unintended interference between these two triplets happens. In addition, the wave-vector difference of two Raman beams  $\delta\mathbf{k}$  has to have a component along the hopping direction ( $\mathbf{v}$ -direction in this case) to ensure the Raman-assisted hopping strength is non-vanishing [70].

Since the real-space Hamiltonian contains hopping terms along nine different directions and each of them requires a similar configuration as above, the overall scheme necessitates a considerable number of laser beams. Although many of the beams can be used in common and created from the same laser by an electric or acoustic optical modulator, the implementation is nonetheless very challenging. A simpler implementation protocol of Hopf insulators is highly desired. Controlled periodic driving may be a promising alternative. Also, theoretically it may be possible to find a more natural model Hamiltonian that encapsulates the nontrivial Hopf physics, which may in turn simplify the experimental realization. We would like to emphasize, however, our detection and measurement protocol do not depend on the particular realization scheme. Regardless of the specific implementation of Hopf Hamiltonians, we can detect the Hopf invariant and probe the rich knot structures hidden in Hopf insulators.

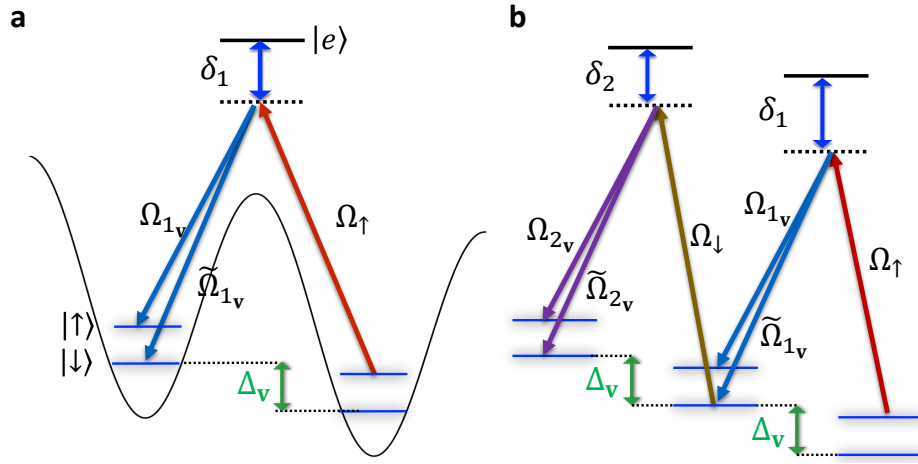


FIG. S1. **Laser configurations.** Schematics of the laser configuration to realize the Hamiltonian  $H_v$ . (a) A linear tilt  $\Delta_v$  per site along the  $\mathbf{v}$  direction is imposed. A Raman triplet with detunings matching the frequency offset can induce spin-flip hoppings in a desired direction. (b) Two Raman triplets that realize all hoppings in  $H_v$ .  $\delta_1$  and  $\delta_2$  are two different detunings from the excited states. The Rabi frequencies for each beam in terms of the unit  $\Omega_0$  are:  $\tilde{\Omega}_{1v} = -\sqrt{2}\Omega_0 e^{i\pi/4} e^{-ikx}$ ,  $\Omega_{1v} = -\Omega_0 e^{-ikx}$ ,  $\Omega_{\uparrow} = \Omega_0 e^{iky}$ ,  $\tilde{\Omega}_{2v} = \sqrt{2}\Omega_0 e^{-i\pi/4} e^{-ikx}$ ,  $\Omega_{2v} = \Omega_0 e^{-ikx}$ , and  $\Omega_{\downarrow} = \Omega_0 e^{iky}$ , where  $k$  is the magnitude of the laser wave vector. All these Raman beams can be drawn from a single laser through an electric or acoustic optical modulator.